



Assessing thermal properties of multipass weld beads using active thermography: microstructural variations and anisotropy analysis

Raffaella Sesana¹ · Luca Santoro¹ · Francesca Curà¹ · Rosario Molica Nardo² · Piergiorgio Pagano³

Received: 14 April 2023 / Accepted: 12 July 2023
© The Author(s) 2023

Abstract

In the present paper, the results of a research focused on microstructure investigation of steel welded joints by means of non destructive thermographic technique are presented. In particular, two rough joints obtained by means of irregular manual welding are analyzed. Active lock in thermography phase analysis is applied, basing on the evidence that thermal diffusivity is related to the thermal diffusion length, using the phase contrast trend as a function of the distance from the laser spot. Diffusivity is expected to be dependent on the local microstructure and vary through different directions. By the variation in diffusivity, it is possible to investigate the level of anisotropy. The results are compared with micrographic analysis. The proposed method provides an active lock-in infrared thermography analysis by means of a thermal camera and an exciting laser head to evaluate thermal diffusivity.

Keywords Active thermography · Welded joint · Microstructure

1 Introduction

Welded joints are commonly used for mechanical, non-removable joining of components. Properties of welded joints can be affected by various factors, including inappropriate selection of welding parameters, incorrect preparation, and inadequate cleaning of the weld grooves. The presence

of flaws, such as pores or cracks, can significantly impact the mechanical properties of welded joints, including fatigue life and tensile strength, so it is important to detect and evaluate them. Mechanisms leading to the formation of flaws are numerous and complex. In recent years, the field of welding research has made significant progress toward improving the quality of welded joints. However, despite these advancements, the formation of defects in welded joints remains a significant challenge. Welding is a complex process, influenced by various physical and chemical phenomena, and even minor deviations from the optimal conditions can lead to the formation of flaws. Understanding the mechanisms responsible for defect formation is, therefore, crucial for developing effective strategies for defect prevention. Several studies have been conducted to investigate the relationship between welding parameters and formation of defects in welded joints. For instance, in his work [1], Filyakov presented the effect of arc instability in defect formation in pipe welding. A topographic map was shown, correlating flaws to the arc interruption zone. A strong relationship between molten pool dynamic phenomena and anomalies present in the weld bead was highlighted. The topography in [1] was the result of an unstable solidification of the weld pool. Similarly, Hong's study [2] proposed a visual sensing algorithm applied to images of the weld bead applied to the climbing helium arc welding process. Again, there was a correlation between melt

All authors are contributed equally to this work.

✉ Raffaella Sesana
raffaella.sesana@polito.it

Luca Santoro
luca.santoro@polito.it

Francesca Curà
francesca.cura@polito.it

Rosario Molica Nardo
rosario.molicanardo@adesndt.com

Piergiorgio Pagano
piergiorgio.pagano@alstomgroup.com

¹ DIMEAS, Politecnico di Torino, Corso Duca degli Abruzzi 24, Torino 10129, TO, Italy

² ADES Group, Via della Pentapoli 48, Priolo Gargallo 96010, SR, Italy

³ ALSTOM Ferroviaria, via O. Moreno 23, Savigliano 12038, CN, Italy

pool solidification and defect creation. In Nguyen's study [3], another analysis of weld pool dynamics and flaws was presented, where by analyzing the molten flows, it was possible to retrieve bead dimension, lack of penetration, burn trough, and humping. Most of the flaws originate in the weld pool (pores, hot cracks) or in its proximity due to the multiple physical and chemical processes. As a matter of fact, discontinuities in the process introduced by an irregular arc, improper preparation of the welding groove (bad milling, contaminated surface), an improper pre-post heat treatment, or more generally by a non-correct process parameter setup can lead to defect formation [4]. In an industrial approach, it is common to use non-destructive tests at different processing steps to check the quality of a joint. For example, Aucott [5] presented an online radiography study to hot crack formation. However, the most important parameters to be monitored were microstructure and residual stresses. It was crucial to assess the welding procedure to avoid brittle phases such as martensite or high stresses, which can lead to premature failure of the welded joint. In technical literature, several researchers have focused their efforts on thermographic testing and monitoring methods. Thermography is a non-contact technique that can be used to obtain thermal maps of a component surface during an observation period. In its latest applications, a new approach called active (or stimulated) thermography is providing interesting results. Active thermography is a diagnostic tool that thermally stimulates a component by means of an external heat source in order to characterize thermal properties and/or to detect flaws. What is known from this methodology is that the thermal response of a component volume with a defect is different than in sound regions. The thermal stimulation can be classified into two categories: photo-thermal stimulation, which introduces the heat through the surface, and volumetric stimulation, where the heat is produced in the bulk of the material by dissipative phenomena. These techniques are well-suited for offline investigation of welding microstructure and defects detection and were widely applied for composites and laminates [6–8]. For example, Guo et al. [9] used ultrasound stimulation to heat up a component in order to detect cracks. Similarly, Park et al. [10] used ultrasound thermography for microcrack detection in dissimilar metal welds. Active thermography is not only used for defects detection, but can also provide important information about the welded area. Dell'Avvocato et al. [11] used laser stimulation to measure the welded area in resistance projection welding. In [12], the same stimulation was used to assess the microstructural properties of heat-treated steel. Another volumetric stimulation technique is electromagnetic induction. Cheng et al. [13] used an induction system to heat a stainless steel weld. Yuan et al. [14] proposed the induction thermography for condition monitoring of overlay welded components under multi-degradation. One of the main advantages of this

technique is that with proper signal processing, it can give a visual indication of anomalies. In [15], laser, induction, and heat gun stimulation were used to detect defects in nickel superalloy welds. Broberg et al. [16] proposed a crack detection method using laser stimulation, but only surface cracks were detected. The same method was used in [17], except for an additional post-processing using the second temporal derivative in order to mark the crack in the image. The laser was also used in [18] to assess the nugget extensions in the spot-welded joint. Similarly, active thermography using both laser and lamp stimulation was used on Cu solder connections [19]. In thermographic testing, active thermography (AT) was considered. It consists in studying the thermal response of a component subjected to an external heat source, in the present case a laser beam, and the corresponding technique is called laser active thermography. A more traditional approach is represented by passive thermography, a technique in which the thermal response of the material is generated by mechanical stimulation (for example, fatigue loads). This excitation generates dissipative phenomena, and their thermal effects on the component surface are acquired and processed. This technique was successfully applied for progressive damage detection in case of mechanical fatigue in the elastic and plastic fields [20, 21] and for fatigue resistance assessment [22, 23]. Thermography applied to the welding process and application appeared around the 80 of last century. In [24] a wide review of weld geometry measurement by means of different techniques was presented with a paragraph dedicated to IR thermography. In [25] PT was used for real-time monitoring of GTAW and GMAW weld metal cooling rate. Among these preliminary results, it was observed that the effect of emissivity on the accuracy of the temperature measurements was minimized as the oxide coating on the weld metal is rather uniform and therefore exhibited a uniform emissivity. Furthermore, the cooling rate full field investigation was proposed as a technique for defect detection, NDE and process control. In [25] the temperature field of a homogeneous plate undergoing a moving heat source was calculated on and near the bead in laser welding. The results are compared with thermographic and thermocouple measurements. The aim of the research is to control the welding process by thermographic monitoring and to design it by means of analytical simulation. In [26] three types of joints were evaluated and compared by AT and in particular pulse and modulated thermography with optical stimulation. In particular, the variation of the phase angle with excitation frequency was compared for different kind of joints showing the relation between material structure and thermal signal phase in welded joints. In [27] the temperature distribution in longitudinal and transverse weld directions for GTAW joining of SS316L to Inconel625 thick plates multipass welding was related to distortions and induced residual stresses by means of PT. Another interesting application is real-time welding process monitoring. In this

paper, we build upon the work presented in [28] by providing a detailed analysis of defect generation mechanisms in aluminum welded joints. As an extension of [29], the present work aims to apply a similar methodology to study the local thermal properties of a multipass steel welded joint in order to evaluate the microstructural condition and anisotropy. A detailed and deep investigation on the relation of multipass welding process parameters and microstructure of weld deposition is presented in [30] and [31] for metallurgical characterization of multi-track Stellite 6 coating on SS316L substrate. The wide experimental activity presented clearly demonstrated the effect of microstructure on process parameters, for example, the speed of torch oscillation. The present study, aiming at investigating the applicability of AT to non-destructive metallurgical characterization of highly irregular steel weldings, assumes significant implications for the welding industry as it provides valuable insights into the thermal behavior of weld beads with different microstructures. The ability to distinguish between the different microstructures and their thermal properties allows for the optimization of welding procedures to achieve desired microstructures and properties in welds. This is particularly important in industries such as aerospace, automotive, and shipbuilding, where the strength and durability of welded joints are critical. Furthermore, the proposed active thermography method can be extended to other materials and structures, providing valuable insights into the thermal behavior of complex geometries. This method can be applied to other welding techniques such as TIG, MIG, and laser welding, as well as other joining techniques such as brazing and soldering. The potential for this method to be used in various fields, such as metallurgy, material science, and non-destructive testing, is enormous.

2 Materials and methods

To relate thermal IR lock-in measurements to microstructural properties, two welded joints were obtained with different welding procedures. Microstructural analysis and thermographic analysis were performed on base plate material and on weld beads. In particular, the investigated, surfaces were analyzed without surface treatment or finishing, to study the feasibility of this methodology for in-line quality assessment of welding processes (Table 1).

2.1 Specimen preparation

The investigation was run on two steel welded joints which geometry is shown in Fig. 1. The welded plates are made of C30 (1.0528). A weld groove was notched on a 30 mm thick plate with a 60° angle. To achieve a wide range of microstructural and mechanical properties in the two beads, which are crucial for the analysis of thermal properties

Table 1 Specimen preparation parameters

Bead filling technique	String (ST)	Wave (WT)
Preheating	80°C	No
Root gap	1–2 mm	2–3 mm
Post heating	400–450°C x 1 h	No
Current level	Optimal	High
Cooling type	Insulated	Waterwashing

and anisotropy of the weld joint, different procedures were applied while processing. The weld parameters were chosen to obtain different microstructures, residual stresses, and deformations in the HAZ (heat affected zone). Two different welding techniques were used to produce the two joints: the string technique (ST) and the wave technique (WT). The ST involves a linear movement of the consumable electrode along the weld path, while the WT uses a different filling technique where the electrode is moved on a wavy path. The ST bead was preheated, while the WT bead was not. This allowed for steeper cooling transients for the WT bead. Additionally, the ST bead was subjected to post-weld heat treatment and insulated cooling, while the WT bead was water-washed after welding. The root gap was larger for the WT bead, to obtain further increase of the heat input and higher distortions and anisotropy of the weld bead due to asymmetric grain growth.

2.2 Microstructural analysis

Since the different thermal properties measured in the weld bead are related to different microstructures, a microstructural analysis was performed in order to validate the thermographic results. To this aim, specimens of the weld joint cross-sections were polished using $1\ \mu\text{m}$ diamond paste. Then, the polished surface was etched with Nital 2% solution. Micrographic specimens were cut in the center of the weld bead and the analysis was performed on the surface perpendicular to the axis of the joint. A reference system was set on specimens (Fig. 2) where X is the welding axis direction and Y is the perpendicular direction. In base material specimen, X direction identifies the lamination direction while Y the perpendicular direction.

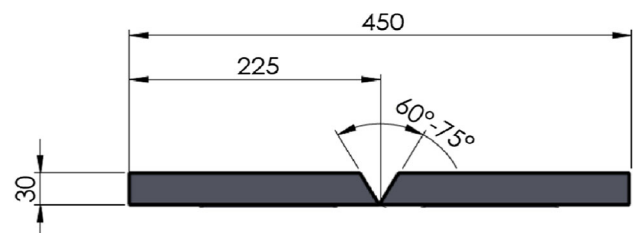


Fig. 1 Specimen preparation with weld groove

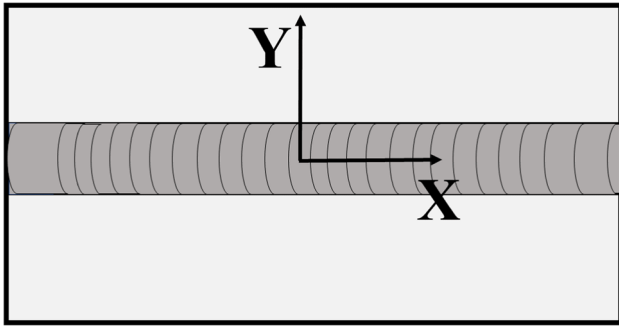


Fig. 2 Reference system on the welded joint

2.3 Experimental thermographic setup

The thermographic analysis was performed on rough specimen surfaces. A laser-active thermography was considered for the present investigation. The experimental equipment was composed of a thermal camera, a laser excitation source, and a PC control unit. The IR thermal camera is a FLIR A6751sc with a sensitivity lower than 20 mK and 3–5 μm spectral range, while the laser source can generate a maximum power of 50 W concentrated in a circular spot of a diameter of 2 mm. The experimental configuration was set in reflection mode as shown in Fig. 3. The Lock-In thermography involves the application of repeated step pulses modulated at a specific modulation frequency, the *lock-in frequency*. This technique allows for more advanced signal processing, in phase and frequency, resulting in more consistent and accurate results. In the present research, one lock in frequency was applied, 1Hz, and 25 pulses with a laser power corresponding to 7.5W. The emissivity was measured by means of a Timage Radiamatic MK3 thermal camera, a

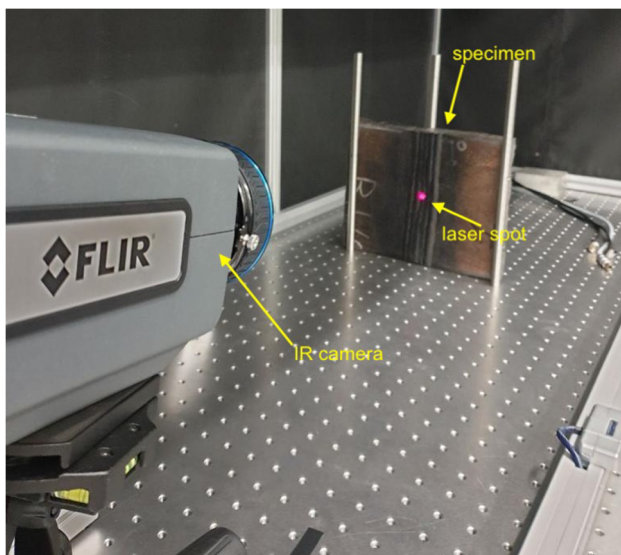


Fig. 3 Thermographic testing set-up

Table 2 Thermographic FOV setting

HFOV	VFOV	IFOV
200 mm	160 mm	0.32 mm

thermocouple, and a heat-gun, according to Standard ASTM E1933-18. The experiments were run at 26.0°C room temperature, relative humidity 30% and a distance between the laser source and the target of 530 mm. With this setup, the parameters regarding the Field of View are presented in Table 2. In Table 3 the lock-in parameters set up is reported.

2.4 Thermographic data post-processing

As regards, the specimen surface emissivity, it was assessed for active thermography testing according to Standard ASTM E1933-18. The specimen surface was heated with the heat gun until a stationary temperature was reached and monitored with the thermocouple. Therefore the emissivity in the thermal camera software (TImageConnect) was set in order to read the surface temperature acquired by the thermal camera equal to the one read with the thermocouple. This procedure is allowed for temperature increment lower than 400 °C [32] when a change in emissivity is observed in steel surface, generally related to the surface state [33]. In the present case, the increment generated with the heat gun was 80 °C and the obtained emissivity, by means of 3 repeated tests, was 0,55. To further ensure accuracy and consistency of results, a special attention was paid to laser power and acquisition frame rate. The laser power was carefully adjusted as suggested in the literature to avoid high surface temperature increment which could cause non-linearities [34] in the thermal diffusive phenomena. Meanwhile, the acquisition frame rate was optimized to obtain the smallest number of frames per test, while still maintaining an elevated time resolution. In particular, in the present case, the thermal camera frame rate was set to 60Hz. This consistency in testing methodology allowed for an accurate comparison of the results obtained on the specimens (Table 3).

The theoretical and signal processing procedure is presented in the following. The thermal contour sequences, acquired during the lock-in test, were post-processed to obtain both phase and amplitude plots of the thermal contours in time. Before processing the related information, the data were denoised using a singular value decomposition (SVD) denoising algorithm, which reduces the noise in the

Table 3 Experimental parameter

Modulation Frequency	N° of pulses	Power	Frame rate	Range
0.5Hz	25	7.5W	60Hz	0-90°C

phase signal for low-thermal amplitude pixels [35]. Phase and amplitude data of the thermal signal were extracted with a dedicated Matlab routine by means of the Fast Fourier Transform (FFT), performing a 1D Fourier transform of the temperature vs time signal related to each pixel. To this aim, data were formatted as a 3D tensor, where the first two dimensions are the spatial ones (pixels) and the third dimension is the time dimension (frames). Then for each pixel, a Fourier transform analysis was performed along the time axis to extrapolate its amplitude and phase contribution. The result was a 3D map plot of the phase and for the amplitude value in each pixel vs time. Similar applications are described in [27, 34, 36–41].

This procedure was generally applied to point out subsuperficial defects in components, as defects can perturbate heat diffusion, as for example in [39, 42, 43]. While for amplitude meaning, a detailed description was reported [44], in this particular case, the phase map has a different application. The plot of the phase value, along an arbitrary axis centered in the target spot, is expected to be linear according to [34] and the linear part of the phase plot corresponds to the diffusion area of heat during the lock-in pulsation. The slope of the linear trend is related to thermal diffusivity according to [34]:

$$m = -\sqrt{\frac{\pi f}{D_x}} \tag{1}$$

where m is the slope [rad/mm] of the linear part of the phase plot, while f is the modulation frequency [Hz] of the laser spot lock-in stimulation and D_x is the thermal diffusivity [mm²/s] along the measured surface direction in which phase/space diagram is plotted by cutting the phase map. The thermal diffusivity is defined as:

$$D_x = \frac{k}{\rho c} \tag{2}$$

where k is the thermal conductivity [W/(m*K)], ρ is the mass density [Kg/mm³], and c is the specific heat [J/(Kg*K)]. The thermal diffusivity along a particular direction can be obtained using the Eq. 1. This methodology allows to obtain thermal diffusivity along any possible direction, avoiding boundary effects, even for small components. It is possible to relate the thermal diffusivity to the diffusion length, using the phase contrast trend as a function of the distance from the laser spot. The thermal diffusion depth μ is defined as the distance that the heat diffuses through the material, undergoing a sinusoidal stimulus, during a time $1/f$. Then, the thermal diffusion length can be related to the slope of the phase in relation to the distance from the laser spot. Generally speaking, the experimental setup does not allow for ideal conditions, that is no noise and an adimensional heat source. Then, to avoid biases and errors, precautions must be taken

when selecting the linear part of the phase plot to estimate the slope, as follows. The phase plot presents in the center a plateau that corresponds to the area heated by the laser spot. Beyond a certain distance from the laser spot, the data becomes noisy due to the low amplitude of the signal. In Fig. 4 the contour phase plot is reported as an example in an instant following the heat impulse. In Fig. 5 an example of the section of a non-denoised phase plot of one investigated sample, according to a generic direction passing through the center of the plot, before processing, is reported as an example. To minimize these noise effects, in the present research, all phase data related to pixels, which temperature value was lower than 0.1 K, were excluded. In Fig. 6 the section of the same phase plot, denoised and processed, is reported as an example. In Fig. 6, the typical trend in the phase plot is evident. It can be divided into two separate regions, which are referred to as A and B. Region A represents the area where the laser beam heats the material and creates a Gaussian-distributed heat flow pulsation, resulting in a plateau on the phase diagram. The extension of this plateau is directly related to the radius of the laser beam spot. On the other hand, region B represents the surface surrounding the laser spot, where thermal diffusion takes place. The center of the circular area of the phase plot, which corresponds to the center of the laser spot, was selected as the origin of a radial coordinate system. This procedure allows for minimizing the impact of any bias or systematic errors in the data.

A linear polynomial fitting of the phase-cut in the area surrounding the laser spot was implemented to obtain the slope of the experimental data to calculate the thermal diffusivity m . In order to estimate the slope of the linear part of the phase plot, for different ROIs or for repeated measurements in the same point, a data processing procedure was defined. The linear trend was assumed to start at a distance from the origin equal to twice the laser spot radius.

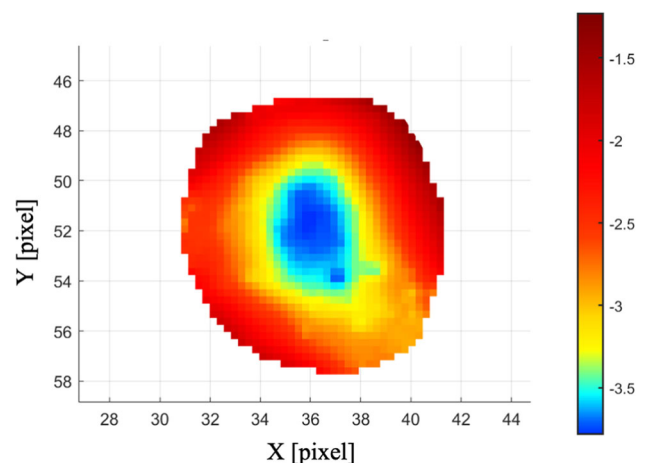
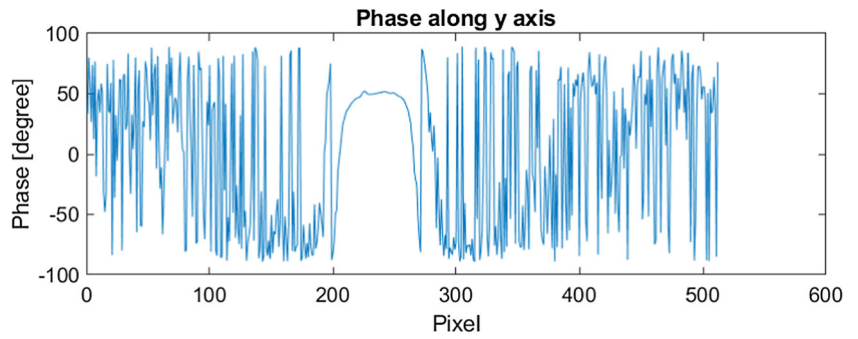


Fig. 4 Wave bead phase map

Fig. 5 Example of rough phase plot cut



Then a routine was defined to estimate diffusivity from phase thermographic data, and it was applied as follows. The diffusivity parameter D is initialized as zero value. Then an initial expected thermal diffusivity $D_{expected}$ is defined as equal to an arbitrary value (for example, 10). With $D_{expected}$ the corresponding estimated thermal diffusion length $\mu_{expected}$ is calculated according to the equation (3).

$$\mu_{expected} = \sqrt{\frac{D_{expected}}{\pi * f}} \tag{3}$$

The estimated thermal diffusion length allows estimating the initial value of the extension of the linear trend r_{ext} , centered in the center of the spot, as

$$r_{ext} = 2 * r_{laserspot} + 2 * \mu_{expected} \tag{4}$$

$\mu_{expected}$ permits to uniquely define the interval where the initial fit is run, that is in within these bounds:

$$[2 * r_{laserspot}, 2 * r_{laserspot} + 2 * \mu_{expected}] \tag{5}$$

Then, in the interval between r_{spot} and r_{ext} , the slope of the approximated linear part of the plot was calculated and the fitting estimation D_{fit} is obtained. The goodness of the fitting is quantified by means of the R^2 of the approximation. If it is acceptable, that is below a given threshold value, then D becomes D_{fit} and the difference between D and $D_{expected}$ compared to a threshold value which depends on the problem and defines the convergence of the problem. According to this last test, the following iteration can improve the estimation

or it is stopped. In the reported Algorithm 1 the iteration is presented. In the present tests, the modulation frequency f is 1Hz (modulation period $T=1$ s), and the diffusivity value are calculated along X and Y directions, where X is along the weld bead axis and Y is perpendicular, as reported in Fig. 2. Three thermal lock-in acquisitions were run on the base material, WT, and ST material. In each site, three repetitions were measured and processed.

In Fig. 7, the fitting obtained on the linear part of the phase-cut is reported as an example, where the algorithm gave $R^2 > 0.99$. In particular, the dotted curve represents the denoised experimental phase data for an investigated specimen, that is the phase data of a line obtained by intersecting the phase plot with a plane parallel to X or Y axis, through the center of the spot and perpendicular to the XY plane. The continuous curve represents the regression line obtained by means of the fitting algorithm reported in Algorithm 1. The slope of this fitting curve is used for calculating the thermal diffusivity of the corresponding specimen.

3 Results and discussion

3.1 Micrographic analysis

The microstructural analysis of the weld cross-sections revealed important insights into the thermal behavior of the welding process. The microstructure of the weld bead is directly related to the cooling rate and the heat input during the welding process. Furthermore, the microstructural analysis can also provide information on the mechanical properties

Fig. 6 Example of denoised phase plot cut

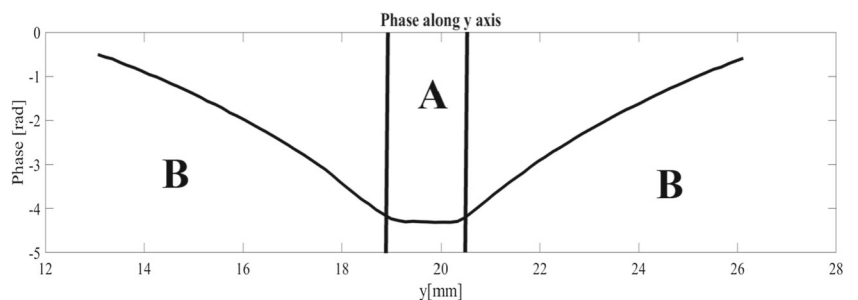
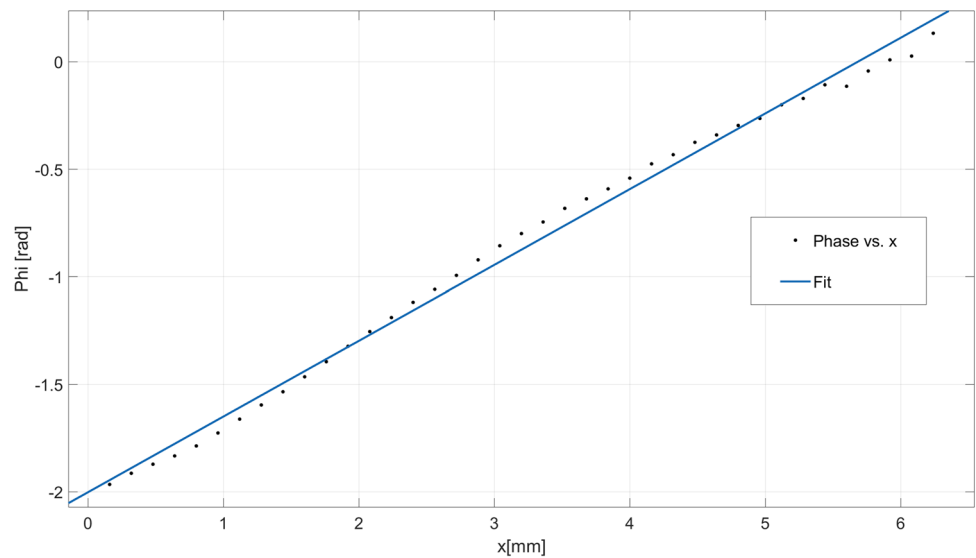


Fig. 7 Fitting line (continuous) and experimental data (dotted) for phase plot



Algorithm 1 Calculate thermal diffusivity

- 1: Find the center of the laser spot in the phase diagram
 - 2: Cut_x and Cut_y as the phase plots in directions parallel respectively to the x and y axis and passing through the center.
 - 3: Define an expected thermal diffusivity D_{exp} , the radius of the laser spot r , and the modulation frequency of the laser f
- Require:** $D_{exp} \geq 0$ and $r_{spot} \geq 0$ and $f \geq 0$
- 4: $\mu_{exp} = \sqrt{\frac{D_{exp}}{\pi f}}$
 - 5: $r_{start} = 2 * r_{spot}$
 - 6: $r_{end} = r_{start} + 2 * \mu_{exp}$
 - 7: $D=0$
 - 8: **while** $|D - D_{expected}| > 2mm^2/s$ **do**
 - 9: execute Matlab fitting algorithm along Cut_x and Cut_y to calculate D_{fit}
 - 10: **if** $R^2 > 0.99$ **then**
 - 11: $D = D_{fit}$
 - 12: **end if**
 - 13: **if** $|D - D_{expected}| < 2mm^2/s$ **then**
 - 14: Diffusivity measurement is reliable
 - 15: **else**
 - 16: Change D_{exp} with D
 - 17: **end if**
 - 18: **end while**

of the weld beads. The inferior bainite microstructure of the ST weld bead, for instance, is known for its excellent toughness while the martensitic microstructure of the WT weld bead provides high strength and lower toughness. The different microstructural characteristics observed in the base material and the weld bead provided a clear indication of the changes which occur during the welding process.

The base material microstructure (Fig. 8a) is mainly pearlitic and ferritic, as expected for a laminate material. The microstructure of the weld bead, on the other hand, is highly dependent on the welding procedure specifications. The ST weld bead (Fig. 8b), for instance, exhibits a typical inferior bainite microstructure, while the WT weld bead

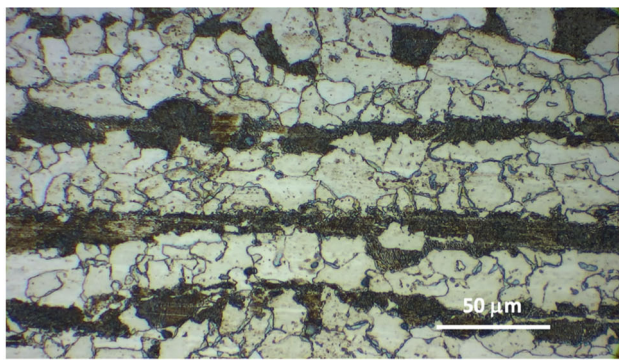
(Fig. 8c) is completely composed of martensite. The differences in the microstructural composition of the weld beads indicated the different cooling rates and heat inputs of the welding procedures. The ST weld bead, for instance, had a slower cooling rate and lower heat input than the WT weld bead. These observations are significant in understanding the thermal behavior of the welding process and can be used to optimize the welding procedures for specific applications.

3.2 Thermographic analysis

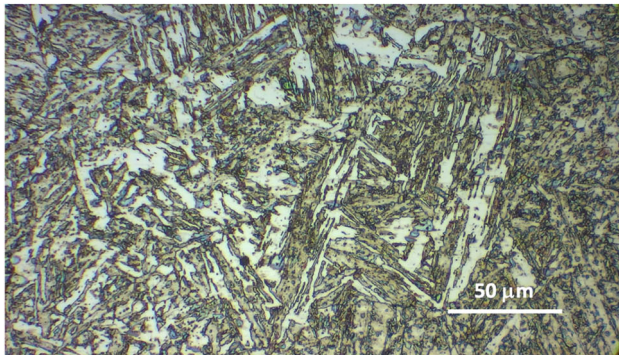
Different measurements were conducted to assess the variability of the properties in the two weld beads and in the base material. The measured thermal properties, obtained by means of thermographic technique are discussed with respect to microstructural analysis.

Table 4 presents the results of thermal diffusivity obtained by means of phase thermographic measurement. The columns indicate the three measurement repetitions (1,2,3) on each specimen along each axis and the corresponding average of the three measurements along with the variance. The rows present the diffusivities measured along the X direction, Y direction, the average of the X and Y measurement, and the R-square of the linear fitting along the X and Y axis.

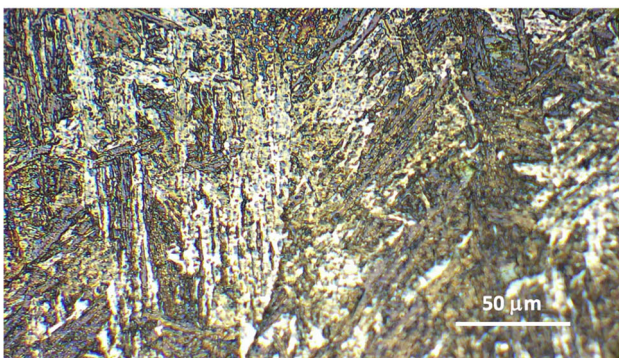
As reported in [29], the expected thermal diffusivity value for boron steel was approximately $15 mm^2/s$, $11.3mm^2/s$ for the martensitic phase and the pearlitic-ferritic base material. In the present work, the measurements were conducted on a weld bead on a plate, so there are different phases within the same specimen that could influence the measured values. The average diffusivity value for the base material was found to be $13 mm^2/s$, for the ST bead was $14 mm^2/s$, and for the WT bead was $11.7mm^2/s$.



(a) Base material microstructure



(b) ST bead microstructure



(c) WT bead microstructure

Fig. 8 Microstructures microscopy views

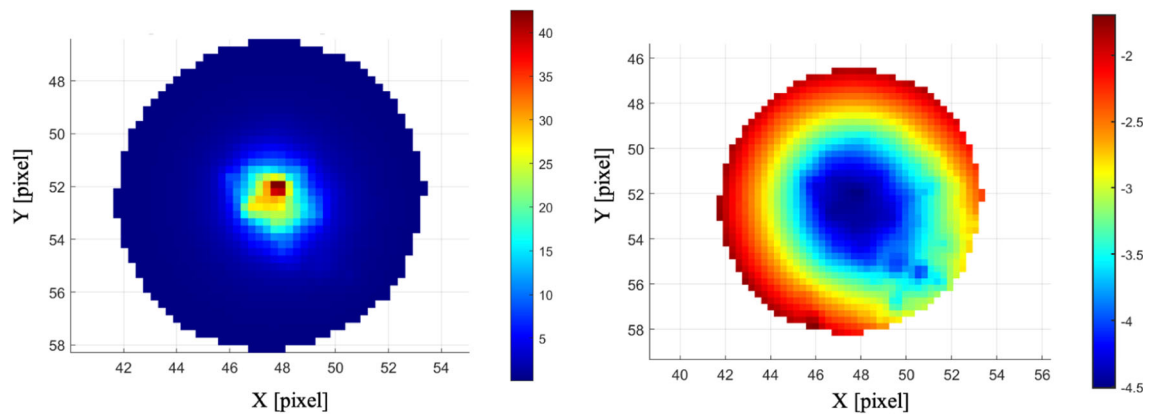
The WT bead, which shows a martensitic microstructure, presents a reduced diffusivity compared to the ST, bainitic, and base material, pearlitic, and ferritic. The martensitic bead has a diffusivity value that is similar to the martensitic plate studied in [29], while the other two values are more similar to the pearlitic-ferritic plate of [29].

It is important to note that the beads were made using a multipass technique to create a thick bead, and the wave bead passes were obtained by moving the consumable electrode also in the Y direction, creating a geometrically and metallurgically irregular bead. This effect was pointed out by a higher scatter in the diffusivity measurements of the WT wave bead, if compared to the other measurements.

Another interesting observation that can be made thanks to this methodology is the anisotropy of the material. The phase method allows for conducting local directional measurements of thermal diffusivity. An eventual anisotropy can be seen as a different slope of the phase along the measurement axis or, graphically, as an ovalization of the shape of the phase map. In this case, it can be seen that the X -axis has a higher thermal diffusivity for all the specimens. A similar result can be observed in Fig. 9 for what concerns amplitude anisotropy it was discussed in [[44]] and it can be related to residual stresses.

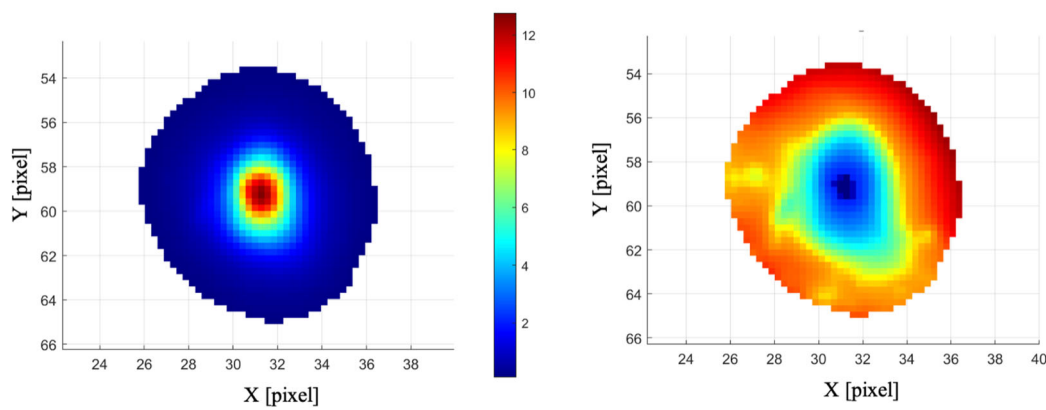
Some further comments are required on Table 4. The diffusivity values measured on all surfaces and in the two directions showed elevated R^2 and variances lower than 2% apart for WT acquisitions. This means that for base material and ST the algorithm to obtain the values works well and a linear trend was clearly identifiable in all the acquisitions. In the case of WT the largest variance was approximately 10% for measurements in X direction, that is along the welding axis direction, but R^2 remained elevated; thus means that a trend is present but the results are scattered. For ST the relative variance is lower than for base material. This can be due to surface oxidation of the base material surface. For base material, ST and WT, diffusivity showed higher values along X direction than along Y . For what concerns base material this difference may be due to the lamination process which stretches the metal crystals in the lamination direction; for ST and WT the difference can be due to the boundary effect between the HAZ and the welded plate: this sort of interface somehow obstacles the diffusion of heat in the Y direction. On the other hand, the scattering of the relative variance of the results for base material and ST can be compared while it is evidently larger for WT measurements. Again this difference can be related to irregularities of the WT surface.

Comparing average values and diffusivity scattering of base material, ST and WT (Fig. 10), it is evident that diffusivity measurements, obtained by means of lock-in active thermographic measurements, point out different microstructures underneath the investigated surface for inferior bainite and martensite structures. That is the average results obtained on ST, confirmed by microstructural analysis, can be clearly distinguished from WT results. On the other hand, the thermal diffusivity measurements of mixed ferrite and perlite base material have given the same results of martensite WT microstructure, then it was difficult to distinguish the two microstructures. This result was confirmed by [45] where the influence of torch oscillation in generating a complex microstructure of an overlay deposition with the PTA welding process is reported. This result was partially overcome by observing that measurements along Y direction allow us to distinguish the different diffusivities and then microstructures.



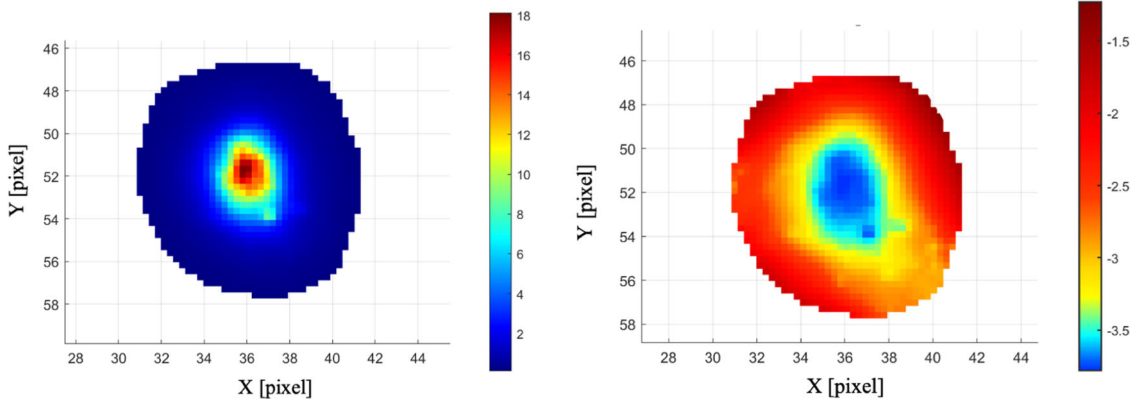
(a) Base material amplitude map

(b) Base material phase map



(c) ST amplitude map

(d) ST phase map



(e) WT amplitude map

(f) WT phase map

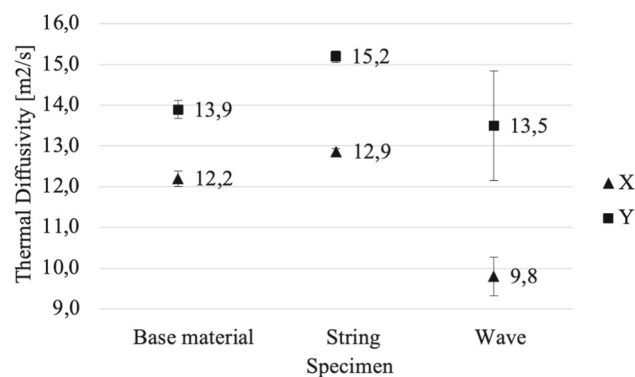
Fig. 9 Phase and amplitude maps for base material, WT and ST specimens

Table 4 Diffusivity results obtained by means of lock-in thermal analysis [m^2/s]

		1	2	3	avg	variance/2	% relative variance
Base Material	x	14.4	13.9	13.3	13.9	0.2174	1.56
	y	12.6	12.2	11.7	12.2	0.1898	1.56
	avg	13.5	13.1	12.5	13.0	0.2023	1.56
	R^2_x	0.9976	0.998	0.9984	1.0	0.0002	0.02
	R^2_y	0.9971	0.997	0.9979	1.0	0.0002	0.02
ST	x	15.6	15.2	14.9	15.2	0.1415	0.93
	y	13.0	12.9	12.7	12.9	0.0642	0.50
	avg	14.3	14.0	13.9	14.0	0.0946	0.68
	R^2_x	0.9983	0.9983	0.9984	1.0	0.0000	0.00
	R^2_y	0.9987	0.9991	0.9985	1.0	0.0001	0.01
WT	x	15.5	15.3	9.7	13.5	1.3548	10.04
	y	10.4	10.6	8.5	9.8	0.4671	4.77
	avg	12.9	12.9	9.1	11.7	0.9106	7.78
	R^2_x	0.9963	0.997	0.9982	1.0	0.0008	0.08
	R^2_y	0.9912	0.993	0.9995	1.0	0.0036	0.36

4 Conclusions

This research aimed at investigating the possibility to detect the microstructure of the weld bead by measuring the thermal properties of the bead by means of a non destructive technique, that is infrared active thermography. This kind of research was already investigated in other reports and the novelty of this paper consists in the technique applied to raw welding surfaces. In particular, the proposed active thermography method was employed to assess the thermal properties of weld beads made by a multipass technique on a plate. The results presented in this paper demonstrated that the proposed method can distinguish differences in thermal properties related to microstructural variations, even on rough surfaces. Specifically, the wave bead, with a martensitic microstructure, exhibited a reduced diffusivity compared to

**Fig. 10** Thermal diffusivity along X and Y directions for different specimens

the string, bainitic, and base material, pearlitic, and ferritic. In particular, the NDE and investigation of HAZ both considering geometry and microstructure in complex geometries can present interesting applications in mechanical and aerospace fields. In summary, this study has demonstrated the potential of active thermography as a non-destructive testing method for assessing the thermal properties of weld beads. The results obtained in this work can be used to optimize welding procedures to obtain specific microstructures and properties in welds, and the method can be extended to other materials and structures. Implications of this work for the welding industry and other fields are substantial, and further research is needed to fully explore the potential of this method.

Funding Open access funding provided by Politecnico di Torino within the CRUI-CARE Agreement.

Declarations

Conflict of interest The authors declare no competing interests.

Open Access This article is licensed under a Creative Commons Attribution 4.0 International License, which permits use, sharing, adaptation, distribution and reproduction in any medium or format, as long as you give appropriate credit to the original author(s) and the source, provide a link to the Creative Commons licence, and indicate if changes were made. The images or other third party material in this article are included in the article's Creative Commons licence, unless indicated otherwise in a credit line to the material. If material is not included in the article's Creative Commons licence and your intended use is not permitted by statutory regulation or exceeds the permitted use, you will need to obtain permission directly from the copyright holder. To view a copy of this licence, visit <http://creativecommons.org/licenses/by/4.0/>.

References

- Filyakov AE, Sholokhov MA, Poloskov SI, Melnikov AY (2020) The study of the influence of deviations of the arc energy parameters on the defects formation during automatic welding of pipelines. In: IOP Conference Series: Materials Science and Engineering, vol. 966. <https://doi.org/10.1088/1757-899X/966/1/012088>
- Hong Y, Yang M, Chang B, Du D (2022) Filter-PCA-based process monitoring and defect identification during climbing helium arc welding process using DE-SVM. *IEEE Trans Ind Electron* 1343–1348. <https://doi.org/10.1109/TIE.2022.3201304>
- Nguyen HL, Van Nguyen A, Duy HL, Nguyen T-H, Tashiro S, Tanaka M (2021) Relationship among welding defects with convection and material flow dynamic considering principal forces in plasma arc welding. *Metals* 11(9):1444. <https://doi.org/10.3390/met11091444>
- Zhou Q, Rong Y, Shao X, Jiang P, Gao Z, Cao L (2018) Optimization of laser brazing onto galvanized steel based on ensemble of etamodels. *J Intell Manuf* 29(7):1417–1431. <https://doi.org/10.1007/s10845-015-1187-5>
- Aucott L, Huang D, Dong HB, Wen SW, Marsden JA, Rack A, Cocks ACF (2017) Initiation and growth kinetics of solidification cracking during welding of steel. *Sci Rep* 7. <https://doi.org/10.1038/srep40255>
- Bang HT, Park S, Jeon H (2020) Defect identification in composite materials via thermography and deep learning techniques. *Compos Struct* 246. <https://doi.org/10.1016/j.compstruct.2020.112405>
- Huang J, Pastor ML, Garnier C, Gong XJ (2019) A new model for fatigue life prediction based on infrared thermography and degradation process for CFRP composite laminates. *Int J Fatigue* 120:87–95. <https://doi.org/10.1016/j.ijfatigue.2018.11.002>
- Pitarresi G, Cappello R, Capraro A, Pinto V, Badagliacco D, Valenza A (2023) Frequency modulated thermography-NDT of polymer composites by means of human-controlled heat modulation. *Lect Notes Civ Eng* 254 LNCE:610–618. <https://doi.org/10.1007/978-3-031-07258-1-62>
- Guo X, Vavilov V (2013) Crack detection in aluminum parts by using ultrasound excited infrared thermography. *Infrared Phys Technol* 61:149–156. <https://doi.org/10.1016/j.infrared.2013.08.003>
- Park H, Choi M, Park J, Kim W (2014) A study on detection of micro-cracks in the dissimilar metal weld through ultrasound infrared thermography. *Infrared Phys Technol* 62:124–131. <https://doi.org/10.1016/j.infrared.2013.10.006>
- Dell'Avvocato G, Gohlke D, Palumbo D, Krankenhagen R, Galietti U (2022) Quantitative evaluation of the welded area. in Resistance Projection Welded (RPW) thin joints by pulsed laser thermography, p. 26. SPIE-Intl Soc Optical Eng, ??? <https://doi.org/10.1117/12.2618806>
- Dell'Avvocato G, Palumbo D, Palmieri ME, Galietti U (2022) Non-destructive thermographic method for the assessment of heat treatment in boron steel, p. 8 SPIE-Intl Soc Optical Eng, ??? <https://doi.org/10.1117/12.2618810>
- Cheng Y, Bai L, Yang F, Chen Y, Jiang S, Yin C (2016) Stainless steel weld defect detection using pulsed inductive thermography. *IEEE Trans Appl Supercond* 26(7). <https://doi.org/10.1109/TASC.2016.2582662>
- Yuan B, Spiessberger C, Waag TI (2017) Eddy current thermography imaging for condition-based maintenance of overlay welded components under multidegradation. *Mar Struct* 53:136–147. <https://doi.org/10.1016/j.marstruc.2017.02.001>
- García de la Yedra A, Fernández E, Beizama A, Fuente R, Echeverría A, Broberg P, Runnemalm A, Henrikson P (2014) Defect detection strategies in Nickel Superalloys welds using active thermography. QIRT Council, ??? <https://doi.org/10.21611/qirt.2014.028>
- Broberg P (2013) Surface crack detection in welds using thermography. *NDT and E International* 57:69–73. <https://doi.org/10.1016/j.ndteint.2013.03.008>
- Li T, Almond DP, Rees DAS (2011) Crack imaging by scanning pulsed laser spot thermography. *NDT and E International* 44(2):216–225. <https://doi.org/10.1016/j.ndteint.2010.08.006>
- Schlichting J, Brauser S, Pepke LA, Maierhofer C, Rethmeier M, Kreutzbruck M (2012) Thermographic testing of spot welds. *NDT and E International* 48:23–29. <https://doi.org/10.1016/j.ndteint.2012.02.003>
- Maierhofer C, Röllig M, Steinfurth H, Ziegler M, Kreutzbruck M, Scheuerlein C, Heck S (2012) Non-destructive testing of Cu solder connections using active thermography. *NDT and E International* 52:103–111. <https://doi.org/10.1016/j.ndteint.2012.07.010>
- Faria JJR, Fonseca LGA, Faria AR, Cantisano A, Cunha TN, Jahed H, Montesano J (2022) Determination of the fatigue behavior of mechanical components through infrared thermography. *Eng Fail Anal* 134. <https://doi.org/10.1016/j.engfailanal.2021.106018>
- Skibicki D, Lipski A, Pejkowski (2018) Evaluation of plastic strain work and multiaxial fatigue life in CuZn37 alloy by means of thermography method and energy-based approaches of Ellyin and Garud. *Fatigue Frac Eng Mater Struc* 41(12):254–2556. <https://doi.org/10.1111/ffe.12854>
- Curà F, Sesana R (2014) Mechanical and thermal parameters for high-cycle fatigue characterization in commercial steels. *Fatigue Frac Eng Mater Struc* 37(8):883–896. <https://doi.org/10.1111/ffe.12151>
- Curà F, Gallinatti AE, Sesana R (2012) Dissipative aspects in thermographic methods. *Fatigue Frac Eng Mater Struc* 35(12):1133–1147. <https://doi.org/10.1111/j.1460-2695.2012.01701.x>
- Alvarez Bestard G, AbsiAlfaro SC (2018) Measurement and estimation of the weld bead geometry in arc welding processes: the last 50 years of development. *Journal of the Brazilian Society of Mechanical Sciences and Engineering* 40(9). <https://doi.org/10.1007/s40430-018-1359-2>
- Lukens WE, Morris RA, Dunn EC (1981) Infrared temperature sensing of cooling rates for arc welding control by! Technical report
- Meola C, Carlomagno GM, Squillace A, Giorleo G (2004) The use of infrared thermography for nondestructive evaluation of joints. *Infrared Physics and Technology* 46(1–2 SPEC. ISS.):93–99. <https://doi.org/10.1016/j.infrared.2004.03.013>
- Vemanaboina H, Edison G, Akella S (2009) Weld bead temperature and residual stresses evaluations in multipass dissimilar INCONEL625 and SS316L by GTAW using IR thermography and x-ray diffraction techniques. *Mater Res Express* 6(9):0965–9. <https://doi.org/10.1088/2053-1591/ab3298>
- Ardika RD, Triyono T, Muhayat N, Triyono (2021) A review porosity in aluminum welding. *Procedia Structural Integrity* 33:171–180. <https://doi.org/10.1016/j.prostr.2021.10.021>
- Dell'Avvocato G, Palumbo D, Galietti U (2023) A non-destructive thermographic procedure for the evaluation of heat treatment in Usibor®1500 through the thermal diffusivity measurement. *NDT and E International* 133. <https://doi.org/10.1016/j.ndteint.2022.102748>
- Bhoskar A, Kalyankar V, Deshmukh D (2022) Metallurgical characterisation of multi-track Stellite 6 coating on SS316L substrate. *Can Metall Q* 1–13. <https://doi.org/10.1080/00084433.2022.2149009>
- Kalyankar V, Bhoskar A, Deshmukh D, Patil S (2022) On the performance of metallurgical behaviour of Stellite 6 cladding deposited on SS316L substrate with PTAW process. *Can Metall Q* 61(2):130–144. <https://doi.org/10.1080/00084433.2022.2031681>

32. Sadiq H, Wong MB, Tashan J, Al-Mahaidi R, Zhao X-L (2013) Determination of steel emissivity for the temperature prediction of structural steel members in fire. *J Mater Civ Eng* 25(2):167–173. [https://doi.org/10.1061/\(asce\)jmt.1943-5533.0000607](https://doi.org/10.1061/(asce)jmt.1943-5533.0000607)
33. Paloposki T, Liedquist L (2005) Vtt research notes 2299. VTT Tiedotteita - Valtion Teknillinen Tutkimuskeskus 2299:3–81
34. Mendioroz A, Fuente-Dacal R, Apianiz E, Salazar A (2009) Thermal diffusivity measurements of thin plates and filaments using lock-in thermography. *Review of Scientific Instruments* 80(7). <https://doi.org/10.1063/1.3176467>
35. Epps BP, Krivitzky EM (2019) Singular value decomposition of noisy data: noise filtering. *Exp Fluids* 60(8):1–23. <https://doi.org/10.1007/s00348-019-2768-4>
36. Breitenstein O (c2010) Lock-in thermography : basics and use for evaluating electronic devices and materials / O. Breitenstein W, Warta M, Langenkamp, 2nd ed edn. Springer series in advanced microelectronics. Springer, Heidelberg
37. Honner M, Litoš P, Švantner M (2004) Thermography analyses of the hole-drilling residual stress measuring technique. *Infrar Phys Tech* 45(2):131–142. <https://doi.org/10.1016/j.infrared.2003.08.001>
38. Lopez F, Maldague X, Ibarra-Castanedo C (2014) Enhanced image processing for infrared non-destructive testing. *Opto-Electronics Review* 22(4):245–251. <https://doi.org/10.2478/s11772-014-0202-2>
39. Maierhofer C, Myrach P, Krankenhagen R, Röllig M, Steinfurth H (2015) Detection and characterization of defects in isotropic and anisotropic structures using lockin thermography. *J Imaging* 1(1):220–248. <https://doi.org/10.3390/jimaging1010220>
40. Paoloni S, Tata ME, Scudieri F, Mercuri F, Marinelli M, Zammit U (2010) IRthermography characterization of residual stress in plastically deformed metallic components. *Appl Phys A: Mater Sci Process* 98(2):461–465. <https://doi.org/10.1007/s00339-009-5422-9>
41. Roemer J, Pieczonka L, Agh U, Gõmiczo-Hutnicza A, Robotyki K, AlMA (2014) Laser spot thermography of welded joints. Technical Report 2
42. Doshvarpassand S, Wu C, Wang X (2019) An overview of corrosion defect characterization using active infrared thermography. Elsevier B.V. <https://doi.org/10.1016/j.infrared.2018.12.006>
43. D'Accardi E, Palumbo D, Tamborrino R, Galietti U (2018) A quantitative comparison among different algorithms for defects detection on aluminum with the pulsed thermography technique. *Metals* 8(10). <https://doi.org/10.3390/met8100859>
44. Curà F, Sesana R, Corsaro L, Filos IP, Santoro L (2021) Lock-in thermography for residual stresses investigation in steel welded joints. In: *Structural Integrity TIC* (ed.) pp. 158. The International Conference on Structural Integrity, ???
45. Kalyankar V, Bhoskar A (2021) Influence of torch oscillation on the microstructure of Colmonoy 6 overlay deposition on SS304 substrate with PTA welding process. *Metall Res Tech* 118(4):406. <https://doi.org/10.1051/metal/202104>

Publisher's Note Springer Nature remains neutral with regard to jurisdictional claims in published maps and institutional affiliations.